A robust coregistration method for *in vivo* studies using a first generation simultaneous PET/MR scanner

Thomas S. C. Ng and Daniel Procissi
Biological Imaging Center, Beckman Institute, California Institute of Technology, Pasadena, California 91125

Yibao Wu
Department of Biomedical Engineering, University of California–Davis, Davis, California 95616

Russell E. Jacobs[a)]
Biological Imaging Center, Beckman Institute, California Institute of Technology, Pasadena, California 91125

(Received 20 November 2009; revised 17 February 2010; accepted for publication 3 March 2010; published 12 April 2010)

Purpose: Hybrid positron emission tomography (PET)/magnetic resonance (MR) imaging systems have recently been built that allow functional and anatomical information obtained from PET and MR to be acquired simultaneously. The authors have developed a robust coregistration scheme for a first generation small animal PET/MR imaging system and illustrated the potential of this system to study intratumoral heterogeneity in a mouse model.
Methods: An alignment strategy to fuse simultaneously acquired PET and MR data, using the MR imaging gradient coordinate system as the reference basis, was developed. The fidelity of the alignment was evaluated over multiple study sessions. In order to explore its robustness *in vivo*, the alignment strategy was applied to explore the heterogeneity of glucose metabolism in a xenograft tumor model, using ^{18}F-FDG-PET to guide the acquisition of localized ^{1}H MR spectra within a single imaging session.
Results: The alignment method consistently fused the PET/MR data sets with subvoxel accuracy (registration error mean=0.55 voxels, $<$0.28 mm); this was independent of location within the field of view. When the system was used to study intratumoral heterogeneity within xenograft tumors, a correlation of high ^{18}F-FDG-PET signal with high choline/creatine ratio was observed.
Conclusions: The authors present an implementation of an efficient and robust coregistration scheme for multimodal noninvasive imaging using PET and MR. This setup allows time-sensitive, multimodal studies of physiology to be conducted in an efficient manner. © *2010 American Association of Physicists in Medicine*. [DOI: 10.1118/1.3369447]

Key words: magnetic resonance imaging (MRI), positron emission tomography (PET), hybrid systems, small animal imaging, *in vivo* biological monitoring

I. INTRODUCTION

Noninvasive, multimodal imaging is increasingly being adopted for both clinical and preclinical studies, as researchers realize that information available from different image contrasts can complement each other to provide more insights into physiological processes of intact, living animals.[1–5] The most prominent example of this has been the widespread adoption of combined positron emission tomography (PET) and computed tomography (CT) systems. Anatomical information from the CT has been very useful in giving context to the PET image, especially in oncology research.[6–9] In both clinical and small animal PET/CT systems, a combination of careful hardware alignment along with image registration via fiducial markers, phantoms, and/or matching of expected uptake patterns in the two images allows accurate spatial fusion of PET and CT images.[10–13]

Magnetic resonance (MR) imaging is another imaging modality widely used for noninvasive, *in vivo* imaging. It can provide high resolution, soft tissue details, along with functional and metabolic information via techniques such as blood oxygenation level dependent (BOLD) imaging,[14] diffusion,[15] and spectroscopy.[16] Recognizing the complementary nature of PET and MR information, especially the utility of the information from multimodal images acquired simultaneously,[17] researchers have developed hardware for hybrid PET/MR systems. Approaches range from MR-compatible PET systems using avalanche photodiode (APD) technology for simultaneous PET/MR imaging,[18,19] a split magnet that can house current state of the art PET detector systems,[20] to field-cycling approaches that allow PET and MR images to be obtained sequentially.[21]

As the combined PET/MR technology matures, it is necessary to develop techniques and imaging strategies that maximize the capabilities of such systems to study interesting and novel biological and clinical questions. An important consideration for multimodal systems is a robust method to merge individual data sets. For small animal PET/CT systems, significant efforts are devoted to ensure good intermo-

dality spatial registration. Two main methods are used: A set of PET and CT visible fiducial markers are imaged with the animal to allow retrospective image registration.[10,13] Alternatively, a registration transform is defined between the fields of view (FOVs) of the PET and CT scanners through judicious design of PET/CT phantoms that span the FOV of both systems, coupled with a reproducible method to position physically the animal holder in both FOVs.[12]

Conceivably, one can adopt similar alignment approaches for PET/MR systems. Two main issues need to be considered specifically in PET/MR systems for spatial alignment purposes. First, the geometry is more constrained in PET/MR than for PET/CT setups. The typical ring diameter for a commercial small animal PET/CT is ~15 cm or greater, compared to 6 cm for the current APD-based PET/MR inserts.[19,22] The animal subject, radiofrequency (RF) coil, and physiological maintenance and monitoring devices need to fit inside this ring. Moreover, to maximize signal to noise ratio (SNR) for MR images, it is often desirable to position the excite/receive RF coils close to the animal. All these factor limit the imaging of fiducial markers concurrently with an animal without specialized invasive approaches.[23] Second, the FOV of the MR is not fixed between scans. An advantage of MR imaging is the flexibility to alter the FOV geometry and resolution of the acquired data depending on the biological region of interest (ROI) within the animal. For example, fMRI BOLD imaging in monkeys and humans often use oblique brain slices to isolate specific functional brain areas; cardiovascular imaging applications may need oblique slices to image structures such as the aortic arch; while dynamic MRI scans may require a tight FOV to obtain sufficient spatial and time resolution. In such cases, we cannot determine the MR imaging FOV *a priori* to facilitate direct PET to MR image alignment. For the purposes of flexible simultaneous PET/MR imaging, we require a reliable strategy to efficiently determine the intersection of the PET and MR FOVs for all scans during the imaging session. Subsequent to the imaging, we also require a method to register the reconstructed PET/MR images to form a multimodal data set.

In a previous study, Judenhofer *et al.*[19] showed that fusion of individual simultaneous PET and MR phantom images using a rigid body transform is possible using an APD-based PET/MR system, with the registration error on the PET/MR image sets after transformation within the spatial resolution of the PET system. This suggests that APD-based PET systems produce images that can be aligned consistently to the MR data sets. In this paper, we extend this observation to develop and evaluate an efficient acquisition and processing setup of simultaneously acquired PET/MR data using a position sensitive APD-based, small animal MR-compatible PET insert. The setup ensures robust spatial alignment of the PET and MR images by first aligning the PET FOV and a fixed MR FOV using a PET/MR visible phantom. The registration accuracy of using a single PET to fixed MR FOV registration for the alignment of images from multiple study sessions was then evaluated. Further, we describe an algorithm to relate multiple MR FOVs to the fixed MR FOV (and hence the PET FOV), harnessing the fact that MR gradients responsible for spatial encoding of images remain fixed throughout all studies. Using the described setup, PET/MR information was acquired in real-time to follow the functional and metabolic status of the *in vivo* tumor microenvironment. Moreover, we show that the setup allows one modality to guide studies with the other within a single imaging session.

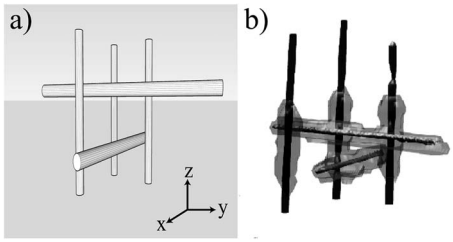

FIG. 1. PET/MR FOV alignment phantom. (a) Rendering of PET/MR phantom. The phantom consisted of five rods, three in the *z*-direction for *xy* plane alignment and two parallel to the *xy* plane for *z* slice alignment. The latter are spaced 5 mm apart. The rods were filled with ^{18}F-FDG solution. (b) PET/MR phantom image overlay. MR image rendering is given as narrow rendered objects (black); PET image rendering is wrapped around the MR rods (light grey).

II. MATERIALS AND METHODS

II.A. MR-compatible PET insert for simultaneous PET/MR studies

Studies were done using a MR-compatible PET insert. The insert consists of a concentric ring of 16 lutetium oxyorthosilicate (LSO) scintillators and position-sensitive avalanche photodiodes (PSAPDs) detector modules. The intact system is designed to fit within the bore of a Bruker Biospin 7T magnet fitted with a Bruker B-GA12 gradient coil set (12 cm i.d., 40 G/cm maximum, 0.2 G cm Å). The FOV offered by this PET setup is $35.35 \times 35.35 \times 12$ mm^3. Previous reports demonstrated little to no interference between the PET and MRI electronics enabling PET and MRI images to be obtained at the same time.[18] PET data were acquired using in-house developed software,[24] while the MR console was run by PARAVISION (Bruker Biospin Inc., Billerica, MA) software. Since the gain of the PSAPD detectors is temperature dependent, the detectors were kept at −12.5 °C for all studies using a continuous flow of chilled dried air.

II.B. PET/MR image alignment

We explored whether alignment using an external phantom can give accurate registration over the course of a study day, as well as over multiple days. An "alignment" phantom consisting of rods filled with ~50 μCi ^{18}F-fluorodeoxyglucose (FDG) solution was imaged simultaneously with both PET and MR. The rods used were glass capillary tubes (OD/ID=1.2/0.68 mm) sealed at the ends with tube sealer (Becton Dickenson, Franklin Lakes, NJ). A model of the alignment phantom is shown in Fig. 1(a). For all PET studies, counts were acquired over 300 s and reconstructed with a maximum *a posteriori* algorithm[25] to a matrix

size of $128\times128\times15$ and a pixel size of $0.276\times0.276\times0.754$ mm^3. MRI images were obtained with a 2D-spoiled gradient echo (FLASH) sequence (TR/TE=350/4 ms) with a matrix size of 128×128, and 40 contiguous slices resulting in a pixel size equivalent to that of the PET images. The FOV of the MR ($35.35\times35.35\times25.6$ mm^3) is larger than the PET ($35.35\times35.35\times12.8$ mm^3) to ensure that the whole PET FOV is captured by the MR FOV and hence allow proper alignment between the two image bases. This MR FOV is denoted hereafter as the home FOV, FOV_{home}. Setting the FOV_{home} as the reference basis, a semi-automatic alignment procedure was adopted to match the two spaces. First, the rod phantoms along the z direction (axial) were matched manually between the PET and MR images. As the spatial resolution of the PET along the axial direction as well as the outer diameter of the rods themselves dictate that one rod in the alignment phantom will traverse multiple PET slices, the central slice of the rod in both PET and MR was used to match the two bases along the z direction. The centroid of the rod cross-sections perpendicular to the z direction served as inputs for alignment in the xy plane. Voxels within five voxels of the local maximum and with intensity above 20% of the local maximal intensity were considered in a center of mass calculation of each centroid. Points were fed into a least-squares 2D affine transformation algorithm implemented in MATLAB.[26] These two steps combine to derive a 3D affine transformation matrix. This matrix obtained at the beginning of the imaging session was stored and used for all subsequent image alignment. We measured the centroid registration error between the MR images and transformed PET images of the alignment phantom using the same transformation matrix over the course of a single day of imaging as well as over several days of imaging, with the centroid of the rod cross-sections on multiple image slices as the metric. The alignment phantom was unloaded and loaded between these scans to simulate a normal *in vivo* imaging session day.

To estimate the positioning accuracy of this alignment scheme as a function of location within the FOV, a phantom consisting of glass capillaries (OD/ID=0.85/0.4 mm), filled with ~50 μCi FDG diluted in 0.05 M Prohance, and located 0, 4, 8, and 12 mm radially from the center of the FOV was imaged simultaneously with PET/MR and aligned using an independently determined transformation matrix derived as above, using the alignment phantom shown in Fig. 1(a). PET/MR images of this phantom are shown in Figs. 2(a)–2(c). The centroid registration error as a function of distance from the center of the FOV was then evaluated as above. One-way ANOVA analysis was used to evaluate whether there were significant differences in registration between rods at different locations within the PET FOV. In Supplemental Material Section I,[27] we compare the alignment accuracy between images acquired with different MRI pulse sequences, with and without the PET insert, demonstrating good geometric matching between images taken with different sequences, also with and without the PET insert. In Supplemental Material Section II,[27] we compare the alignment accuracy between images registered with different transformations, showing that registration with the affine transformation is slightly better than using the rigid body transform.

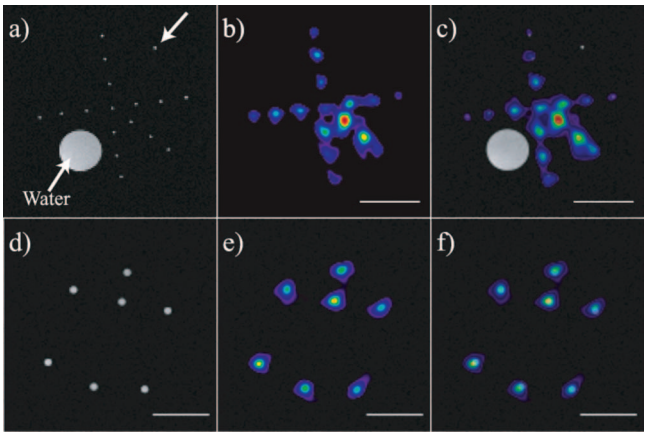

FIG. 2. PET/MR FOV alignment strategy registers other phantom sets robustly. (a)–(c) Structured phantom used to evaluate alignment accuracy as a function of location within the FOV. Rods were located at 0, 4, 8, and 12 mm from the center of the PET/MR FOV. Alignment accuracy was evaluated after registration using a transformation derived from the alignment phantom. (a) MR image of the phantom. (b) PET image of the phantom. (c) Fused data set. A large circular water phantom, shown as the large circle in (a) and (c), was inserted into the phantom to facilitate shim, frequency, and gain adjustments of the MR. One capillary rod was filled with water only and thus was visualized in the MR but not in PET (arrow). (d)–(f) The transform derived to form the overlay in Fig. 1(b) was used to fuse an image containing an alternative phantom arrangement. (f) Fused PET/MR image of a seven rod phantom shows the fidelity of the transform. (Scale bars =10 mm).

The fidelity of this registration scheme was further tested with a third phantom and ^{18}F-FDG studies on mice containing small subcutaneous tumors (MC-38.CEA colorectal adenocarcinoma). Experiments involving the use of animals were done in accordance with protocols approved by the Animal Care and Use Committee of the California Institute of Technology.

II.C. Alignment of multiple MR FOVs

Often it is advantageous to optimize the orientation and size of the MRI FOV to accommodate a specific imaging goal. For simultaneous PET/MR imaging, care needs to be taken to ensure that the alternate MR FOV (FOV_{alt}) overlaps adequately with the PET FOV for the desired region of interest. For quick visualization of the PET and MR FOVs during an imaging session, we use the geometry defined by the MRI metadata to generate Cartesian coordinates of the centroids and vertices for each voxel of both the PET FOV and the alternate MR FOV. These values are used to visualize the "bounding box" of both FOVs in the same coordinate system, which allows a quick determination of the suitability of the FOV_{alt} for PET/MR imaging.

To generate aligned PET/MR data sets, the PET image registered to FOV_{home}, as described in Sec. II B, is first resliced to an isotropic voxel size of $0.276\times0.276\times0.276$ mm^3. It then undergoes a rigid body transformation

using the transformation matrix from MRI metadata, and subsequently resliced to the voxel size of the alternate MR FOV. The whole data stream is implemented in MATLAB; a trilinear interpolation is used for all rotations and reslicing.

To demonstrate the feasibility of this method, we simulated the mapping on phantom images using different geometries that we typically encounter in our studies. An oblique slicing simulating an acquisition along an aortic vessel and a geometry that is offset and sampled at a different matrix size than the home FOV were aligned with simultaneously acquired PET data. This method was also used to remap a PET data set to a mouse anatomical reference image.

II.D. Biological studies with PET/MR: A real-time feedback scheme

TgCEA+C57BL/6 mice ($N=2$) were implanted with MC-38.CEA colorectal adenocarcinoma cells in the groin and shoulder seven days prior to imaging. Mice were fasted 8–12 h prior to the imaging session to minimize extraneous ^{18}F-FDG signals. One hour prior to the imaging session, each mouse was injected intraperitoneally with 200 μCi ^{18}F-FDG. The mouse was then placed in the PET/MRI system and kept at ~37 °C with warm air blowing through the RF coil and anesthetized using 1.5% isofluorane mixed in air. The holder was designed in such a way that the mouse was kept comfortable while the PET insert remained stable at its operating temperature. Using the known alignment matrix, we shifted the expected region of functional interest, in this case the tumor, within the PET FOV using the motorized stage. Once aligned, high resolution anatomical MRI (2D RARE TR/TE=3500/4.5 ms, matrix size=128×128×34, resolution=0.276×0.276×0.754 mm^3) and PET (300 s duration) scans were obtained simultaneously. Both PET and MR images were respiratory-gated to acquire data during the expiration phase.

Alignment time per PET data set was 5–15 min (AMD, 4× Dual-Core Opteron 885 2.6 GHz, 32 GB memory). This relatively rapid calculation time allows processing and analysis of the PET/MR data while the animal is still in the scanner. Analysis of the processed PET/MR images of ^{18}F-FDG uptake within the MC-38 tumors was used to guide the next stage of the experiment. Heterogeneous PET signal within the tumor was verified using ^{1}H MR spectroscopy (MRS). We used the PET signal distribution to delineate ROIs for metabolic studies using ^{1}H MRS (PRESS with VAPOR water suppression, spectral width 8 kHz, 900 averages with 8192 sample points, TR/TE=1685/10 ms, 3×3×3 mm^3, duration=26 min). Three voxels were used for MRS imaging; one in the tumor at the region of high FDG uptake, one in the tumor at a region of low FDG uptake, and one in the contralateral muscle. The resultant spectra were processed and analyzed using Bruker TOPSPIN software (Bruker Biospin, Fremont, CA). A two-sided student's t-test was performed to compare the ratios between the high and low FDG regions.

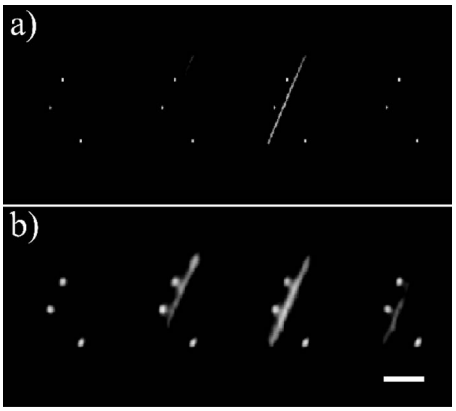

FIG. 3. Different spatial resolution of the PET and MR images. (a) MR xy slices of aligned phantom. (b) PET slices corresponding to (a). Due to the lower spatial resolution of the PET along the axial direction and the positron range in glass matching the thickness of the capillary walls, the rod which was mostly displayed within one slice in the MR image spans almost three slices in the PET image. (Scale bar=10 mm).

III. RESULTS

III.A. PET/MR image alignment

Figure 1(b) shows the overlay of PET and MR surface rendering of the alignment phantom images. Slices along the z axis in Figs. 3(a) and 3(b) show the alignment along both the z direction and in the xy plane and demonstrate the difference in the resolution of the PET and MR images. Rods orthogonal to the z direction span multiple slices in the PET images. This is due to a combination of two factors. First, because the outer diameter of the rods is 1.2 mm and the mean positron range of the glass is ~190 μm annihilation events from the ^{18}F-FDG can occur at the outer edge of the rod, which spans multiple image slices. Second, the spatial resolution of the PET along the axial direction is lower than the image slice thickness (~2 mm). Table I shows the mean and standard deviation of the centroid registration error in all three orthogonal directions for the alignment phantom im-

TABLE I. Centroid alignment error of phantoms using the PET/MR transformation scheme over multiple days. Units are in mm.

	PET/MR alignment phantom									Figure 2(d) phantom	
(mm)	Day 1	Day 1	Day 2	Day 2	Day 2	Day 3	Day 3	Mean	SD	Mean offset	SD
X error	0.22	0.18	0.17	0.15	0.2	0.17	0.17	0.18	0.02	0.18	0.33
Y error	0.15	0.65	0.12	0.1	0.09	0.24	0.11	0.21	0.2	0.11	0.34
Z error	0.09	0.23	0.17	0.18	0.17	0.23	0.27	0.19	0.06	0.21	0.28

TABLE II. Centroid alignment error as a function of location within the transaxial field of view, as measured by the phantom shown in Figs. 2(a)–2(c). ANOVA analysis showed no significant difference in registration accuracy between different locations in the field of view both in the x ($p=0.8$) and y ($p=0.5$) directions. Units are in mm.

	Location from center of PET/MR FOV							
	0		4		8		12	
(mm)	mean	SD	mean	SD	mean	SD	mean	SD
X error	0.12	0.01	0.19	0.13	0.21	0.16	0.28	0.27
Y error	0.19	0.11	0.18	0.12	0.17	0.12	0.24	0.22

ages over the course of one and multiple days. In all directions, registration remained consistently at subvoxel accuracy (maximum mean alignment error=0.21 mm, voxel size=$0.276\times0.276\times0.754$ mm^3) and well within the resolution limits of PET. This alignment procedure ably aligned alternate second rod phantom, as shown in Figs. 2(d)–2(f) and Table I.

Table II shows the registration error as a function of location within the FOV. The alignment remained <0.28 mm in accuracy throughout the whole FOV, with the mean centroid registration error ranging from about 0.18 mm in the center of the FOV to 0.28 mm at 12 mm from the center of the FOV. One-way ANOVA analysis show no significant difference between the mean registration errors at 0, 4, 8, and 12 mm from the center of the FOV in both the x ($p=0.8$) and y ($p=0.5$) directions.

We tested the alignment accuracy *in vivo* by imaging small xenograft tumors. Figure 4 shows aligned mouse PET/MR images at the level of the tumor and heart, with high ^{18}F-FDG uptake in both cases well within the expected anatomical regions.

III.B. Alignment of multiple MR FOVs

Figure 5 shows the MR, PET, and overlaid PET/MR data sets for common geometries used for PET/MR studies. In all cases, voxel grid alignment of the aligned PET images yielded good fit to the MR data set.

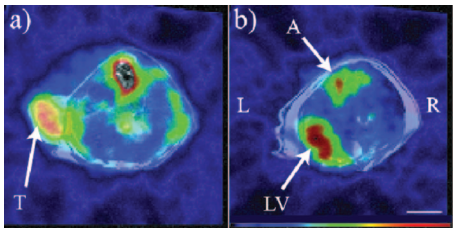

FIG. 4. (a) PET/MR overlaid images at the level of a subcutaneous MC38/CEA+flank tumor showing alignment of high ^{18}F-FDG uptake at the tumor site. (b) Image volume rostral to (a) showing corresponding high ^{18}F-FDG uptake at the left ventricle and aorta (T=tumor, LV=left ventricle, A=aorta, L=left, R=right, V=ventral, scale bar=6 mm).

III.C. Real-time feedback studies with PET/MR allows multimodal imaging of biological processes

Large tumors exhibit heterogeneous structures due to many factors.[28] Figure 6 shows that heterogeneous uptake of the glyolytic marker ^{18}F-FDG is seen within a thigh tumor. This heterogeneity was not readily apparent in the anatomical MR image. To explore this heterogeneity, MRS was obtained in ROIs guided by the variability of ^{18}F-FDG uptake shown in the PET images. ^{1}H MR spectra centered in regions of high ^{18}F-FDG uptake in the tumor showed a higher choline/creatine ratio compared to ROIs in low ^{18}F-FDG areas and muscle (Table III).

IV. DISCUSSION

In this study, we demonstrate the feasibility of performing robust *in vivo* studies with simultaneous PET/MR imaging using a PET insert placed in a small animal MR scanner. Given the spatial constraints within the PET insert and animal holder, a method in lieu of the traditional fiducial marker system is required to ensure robust registration of the two modalities. Once the PET insert is fixed within the MR scanner, the relative orientation of the PET (as determined by the

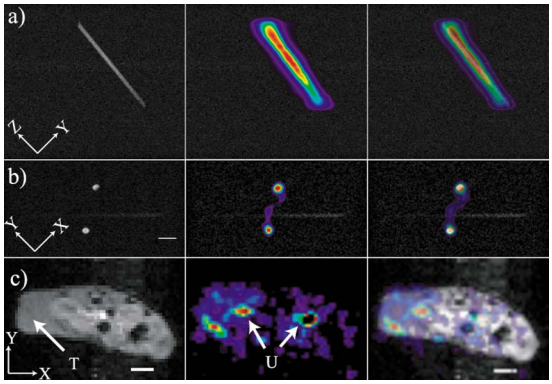

FIG. 5. PET/MR alignment using different geometries. (a) MR slicing of a phantom along the coronal direction, at an oblique angle (40° on the left/anterior plane). (b) MR slicing along the axial direction, rotated 30°. The home coordinate system of the MR gradient set is noted to the left. (c) FDG-PET image of a mouse tumor obtained with axial slices at a FOV ($35\times28\times3$ mm^3) smaller than FOV$_{home}$ ($35.35\times35.35\times25.6$ mm^3). Voxel grid alignment of PET image shows intratumoral heterogeneous uptake while accurately aligning high activity within the ureters. (T=tumor, U=ureters, scale bars=10 mm).

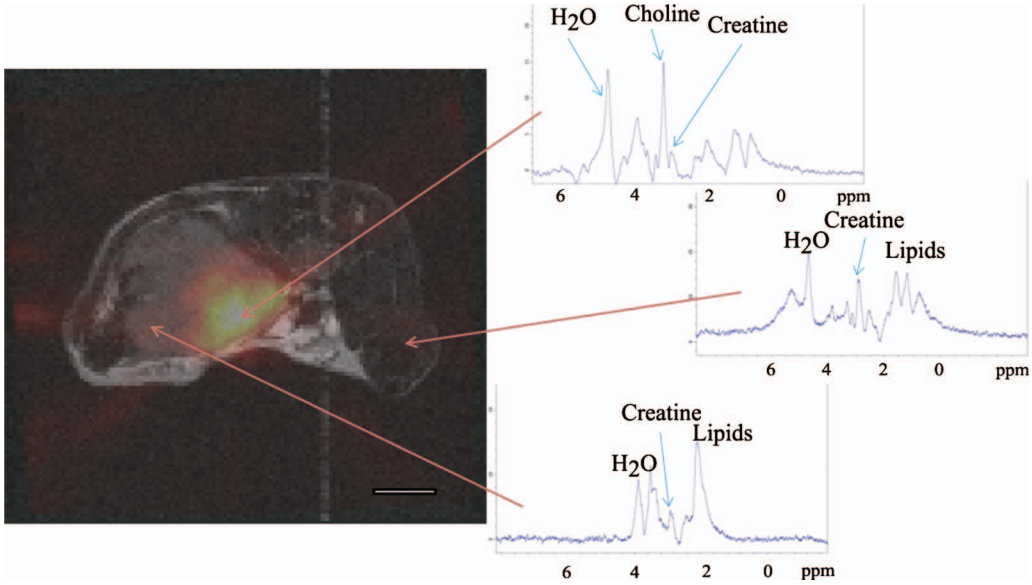

FIG. 6. PET guided MRS assay of MC-38 tumor. Regions of differential ^{18}F-FDG uptake within the tumor were used to define the ROIs for ^{1}H-MRS of the tumor. Spectra show differences between regions of high FDG uptake, low uptake, and contralateral muscle. (Scale bar=3 mm).

placement of the LSO crystal detectors) and MR (as determined by the placement of the imaging gradient set) coordinate systems is also fixed. Thus the transformation matrix that registers images using a single alignment phantom also brings together all subsequent PET/MR images. We confirm this by repeatedly registering the PET and MR images of the alignment phantom over a study session and over multiple days with subvoxel accuracy (Table I) using one transform matrix. This alignment is not dependent on the location within the FOV (Table II). Images of an alternate phantom and tumor bearing mice also support this alignment accuracy (Fig. 4). Straightforward registration of the PET and MR image spaces using a predetermined transformation matrix allows for an uncomplicated multimodal imaging scheme, whereby neither a specially designed PET/MR holder nor an animal mold[23,29] is required for image alignment. This setup provides imaging flexibility; first, there are no potential intensity spillover effects due to an external radioactive marker, which may make low activity ROIs or ROIs close to the marker difficult to discern. Second, this method of alignment allows alternate MRI transmit/receive coil setups to be used without the need for a new alignment scheme, since the registration is based on the spatial encoding provided solely by MR gradient coils. This will be useful for studies that use a surface coil to achieve high SNR. Ideally, the alignment method used should be fully automatic, although previous reports have indicated that partial manual manipulation of images during processing may yield sufficient alignment accuracy.[30] We adopt a manual alignment of the z direction because of the disparate FOV sizes between the PET and MR along that axis. As we make no prior assumption about the physical FOV alignment along this axis, a large MR FOV is taken to ensure full coverage of the PET FOV. From our observations, the removal and replacement of the PET insert within the MR scanner can cause up to 1.5 slices (~1 mm) displacement between the PET FOV and that of the MRI. Studies are in progress to design a phantom alignment setup along the lines of previous designs for PET/CT systems[10,12,13] that will allow fully automated alignment. Nevertheless, the general alignment strategy will remain the same as described here regardless of the phantom setup used.

TABLE III. ^{18}FDG-PET-guided ^{1}H MRS. FDG-PET signal from xenograft tumors (N=2) were used to guide ^{1}H MRS in different PET signal regions. Choline/creatine ratio were significantly different between high and low FDG regions (p=0.02).

Region	Choline/creatine ratio
High FDG tumor region	3.4 ± 0.4
Low FDG tumor region	1.9 ± 0.3
Muscle	Negligible

One notable difference between MR and CT acquisition is the need to alter the imaging geometry in MR to maximize the SNR and to obtain images at the desirable orientation or resolution. This is especially relevant for *in vivo* applications; a compromise must be struck between a realistic scan duration time and the resolution of the acquired image. In MR-only studies, the FOV can only be determined once the animal is loaded inside the scanner. The limited PET FOV adds an extra geometry constraint for PET/MR studies. We have developed a simple software GUI visualizing the overlay of the PET and MR FOVs to allow a quick check to ensure that our anatomical regions of interest lie completely in the useful PET FOV prior to image acquisition.

The constrained geometry of the PET/MR system (which limits the use of external fiducial markers) and the imaging flexibility of the MR require a robust method to coregister PET and MR images with multiple FOV geometries. In previous studies, this has been addressed by making assump-

tions about the anatomical distribution of the functional PET signal,[31–33] using a transmission source or implanting fiducial markers.[23] The first two strategies may not yield an optimal solution if the distribution of the PET signal is unknown or heterogeneous, while the latter is invasive. Given the fact that the PET is fixed physically within the MR during a single imaging session, a simple algorithm was developed that aligns the voxel grids of the "home" PET/MR FOV to any alternate MR FOVs. We make the assumption here that the MR gradients behave consistently between different scans such that the images acquired at a set geometry in software is the same in the hardware. Common Fourier imaging, as described by the *k*-space formalism,[34] relies on spatial encoding determined by spatially and temporally varying magnetic fields created by the MR gradients. Advances in hardware design of gradient coils[35] and post-acquisition processing[36–38] means that most commercial scanners have robust gradient performance, especially for the pulse sequences using Cartesian *k*-space trajectories (see Refs. 39 and 40 for discussion of gradient coil design, specifications, and performance). From a simultaneous PET/MR viewpoint, the pertinent concern is that the presence of the PET insert inside the gradient set may distort the generated gradient fields. Previous characterization of APD-based PET inserts has demonstrated that MR images acquired in the presence of the PET insert show negligible geometric distortions compared to those acquired without the PET[18,19] [see also Supplemental Material Section I (Ref. 27)].

In our implementation, we transform the PET image to match that of the MR images. We chose this approach because the resolution of the PET is lower than the MR, so there would be less potential loss of information from image interpolation. Also, the PET FOV is fixed and typically smaller than the MR FOV, so this approach also simplifies the formation of the fused data set. Other interpolation methods, apart from trilinear interpolation, can be adapted to improve the quantitative value of the transformed images.[41,42] However, the interpolation method we adopted should suffice for PET images. Simulation of some common geometries that require this schema show that the registered PET images align well with the corresponding MR image (Fig. 5). The algorithm described is time efficient; all data sets generated took 20 min or less.

Simultaneous PET/MR imaging allows examination of the different signals in both spatial and temporal registration. In Fig. 6, we see heterogeneity within a tumor microenvironment highlighted with both ^{18}F-FDG PET imaging and high resolution anatomical MRI. ^{1}H MRS, guided by the ^{18}F-FDG signal, confirms the heterogeneous profile of the tumor. Rapid reconstruction, processing, and visualization of the aligned initial PET/MR images provide the information necessary to perform the later MRS study within the same imaging session. Thus, obtaining feedback between the two modalities during a single imaging session is eminently doable with this system. This will have multiple uses. Phantom alignment information allows us to position the mouse to maximize PET signal in the FOV. While new versions of the PET insert will aim to have whole body coverage, this is typically not feasible in clinical systems or in situations where one may want to sacrifice coverage for higher sensitivity and resolution. The feedback schema can also be performed during the experiment to guide study directions. The ability to process and align the PET/MR images quickly within an imaging session allows basic analysis of the combined data set. In our study, this allowed us to determine regions of tumor functional heterogeneity via ^{18}F-FDG accumulations and subsequently, ^{1}H MRS studies, to assess corresponding heterogeneity in metabolite concentration. Again, the external means of image registration proved useful in this situation; no assumption of the expected distribution of the image intensities in either image was used for alignment, allowing us to delineate the heterogeneity within the tumor. Although there is a correlation between the regions of high ^{18}F-FDG uptake and high choline/creatine ratio (Table III), more studies are required to determine the significance of this observation as the relationships between phospholipid metabolism and glycolysis remain unclear.[43–47] Further studies along these lines will involve correlating the tumor characteristics such as perfusion[48] and hypoxia[49] with these functional markers.

Simultaneous PET/MR technology has the potential to impact both preclinical and clinical realms. The time savings that can be obtained by doing two scans at once will facilitate the efficiency of longitudinal studies. Cross-modal image corrections methods such as MR-guided PET motion and attenuation correction, which rely on robust PET/MR coregistration, will improve image quality and aid image interpretation.[50,51] Perhaps more importantly, like the development of multicolor fluorescent proteins and dyes that allow multiple processes to be studied concurrently,[52,53] simultaneous PET/MR will enable similar interactive studies to be done within intact mammalian systems. Molecular imaging agents are being developed with both PET and MR contrast that can look at biological processes such as gene expression,[3] receptor binding,[54,55] cell tracking,[56] and vascular inflammation.[57] Combining these agents within one study will allow multiple physiological processes to be probed simultaneously.

V. CONCLUSIONS

We describe a coregistration design for performing time-sensitive *in vivo* studies using a simultaneous PET/MR scanner. Robust image registration between PET and MR is shown, based on the fixed relative orientation of the PET detectors and MR imaging gradient set. Using this setup, we demonstrate heterogeneous metabolic activity within a tumor using ^{18}F-FDG PET, which was found to correlate with choline/creatine ratios determined using MRS guided by the ^{18}F-FDG signal levels.

ACKNOWLEDGMENTS

The authors thank Dr. Andrew Raubitschek for providing the mice and tumors, Dr. Scott Fraser, Dr. Simon Cherry, Dr. Jinyi Qi, Dr. Ciprian Catana, and Dr. James Bading for advice on imaging issues and support, Hargun Sohi and

Marucha Sanchez for animal handling, Sonia Collazo for computer assistance and Andrey Demyanenko for making the animal RF coil. The project was funded in part by NIBIB Grant No. R01 EB000993, NCRR Grant No. U24 RR021760, Mouse BIRN, a student fellowship from the SNM Education and Research Foundation, and the Beckman Institute.

[a]Author to whom correspondence should be addressed. Electronic mail: rjacobs@caltech.edu

[1]M. Doubrovin *et al.*, "Multimodality in vivo molecular-genetic imaging," Bioconjugate Chem. **15**(6), 1376–1388 (2004).
[2]L. Ottobrini *et al.*, "Molecular imaging: A new way to study molecular processes in vivo," Mol. Cell Endocrinol. **246**(1–2), 69–75 (2006).
[3]P. Ray, R. Tsien, and S. S. Gambhir, "Construction and Validation of Improved Triple Fusion Reporter Gene Vectors for Molecular Imaging of Living Subjects," Cancer Res. **67**, 3085–3093 (2007).
[4]A. Rehemtulla *et al.*, "Molecular imaging of gene expression and efficacy following adenoviral-mediated brain tumor gene therapy," Mol. Imaging **1**(1), 43–55 (2002).
[5]A. Stell *et al.*, "Multimodality imaging: Novel pharmacological applications of reporter systems," Q. J. Nucl. Med. Mol. Imaging **51**(2), 127–138 (2007).
[6]C. la Fougère *et al.*, "Value of PET/CT versus PET and CT performed as separate investigations in patients with Hodgkin's disease and non-Hodgkin's lymphoma," Eur. J. Nucl. Med. Mol. Imaging **33**(12), 1417–1425 (2006).
[7]B. J. Pichler, M. S. Judenhofer, and C. Pfannenberg, *Multimodal Imaging Approaches: PET/CT and PET/MRI*, Handbook of Experimental Pharmacology Vol. 185 (Springer, Berlin/Heidelberg, 2008), Part 1, pp. 109–132.
[8]C. M. Deroose *et al.*, "Multimodality imaging of tumor xenografts and metastases in mice with combined small-animal PET, small-animal CT, and bioluminescence imaging," J. Nucl. Med. **48**(2), 295–303 (2007).
[9]E. Roldán-Valadez *et al.*, "Whole-body (18)F-FDG PET/CT in primary non-Hodgkin's lymphoma of the thyroid associated with Hashimoto's thyroiditis and bilateral kidney infiltration," Rev. Esp. Med. Nucl. **27**(1), 34–39 (2008).
[10]M.-L. Jan *et al.*, "A combined micro-PET/CT scanner for small animal imaging," Nucl. Instrum. Methods Phys. Res. A **569**(2), 314–318 (2006).
[11]P. J. Slomka and R. P. Baum, "Multimodality image registration with software: State-of-the-art," Eur. J. Nucl. Med. Mol. Imaging **36**(1), S44–S55 (2008).
[12]P. L. Chow *et al.*, "A method of image registration for small animal, multi-modality imaging," Phys. Med. Biol. **51**(2), 379–390 (2006).
[13]A. Rodriguez-Ruano *et al.*, "PET/CT alignment for small animal scanners based on capillary detection," in Nuclear Science Symposium Conference Record, 2008 (IEEE NSS '08), 2008 (unpublished).
[14]S. Ogawa *et al.*, "Brain magnetic resonance imaging with contrast dependent on blood oxygenation," Proc. Natl. Acad. Sci. U.S.A. **87**(24), 9868–9872 (1990).
[15]D. A. Hamstra, A. Rehemtulla, and B. D. Ross, "Diffusion magnetic resonance imaging: A biomarker for treatment response in oncology," J. Clin. Oncol. **25**(26), 4104–4109 (2007).
[16]R. J. Gillies and D. L. Morse, "In vivo magnetic resonance spectroscopy in cancer," Annu. Rev. Biomed. Eng. **7**(1), 287–326 (2005).
[17]R. E. Jacobs and S. R. Cherry, "Complementary emerging techniques: High-resolution PET and MRI," Curr. Opin. Neurobiol. **11**(5), 621–629 (2001).
[18]C. Catana *et al.*, "Simultaneous in vivo positron emission tomography and magnetic resonance imaging," Proc. Natl. Acad. Sci. U.S.A. **105**(10), 3705–3710 (2008).
[19]M. S. Judenhofer *et al.*, "Simultaneous PET-MRI: A new approach for functional and morphological imaging," Nat. Med. **14**(4), 459–465 (2008).
[20]A. J. Lucas *et al.*, "Development of a combined microPET-MR system," Technol. Cancer Res. Treat. **5**(4), 337–341 (2006).
[21]G. Bindseil *et al.*, "Design of a combined PET and field-cycled MRI system for small animal imaging," in Proceedings of the 16th Scientific Meeting, International Society for Magnetic Resonance in Medicine, Tokyo, Japan, 2008 (unpublished).
[22]C. Catana *et al.*, "Simultaneous acquisition of multislice PET and MR images: Initial results with a MR-compatible PET scanner," J. Nucl. Med. **47**(12), 1968–1976 (2006).
[23]M. Zhang *et al.*, "Accuracy and reproducibility of tumor positioning during prolonged and multi-modality animal imaging studies," Phys. Med. Biol. **53**(20), 5867–5882 (2008).
[24]M. S. Judenhofer, B. J. Pichler, and S. R. Cherry, "Evaluation of high performance data acquisition boards for simultaneous sampling of fast signals from PET detectors," Phys. Med. Biol. **50**(1), 29–44 (2005).
[25]J. Qi *et al.*, "High-resolution 3D Bayesian image reconstruction using the microPET small-animal scanner," Phys. Med. Biol. **43**(4), 1001–1013 (1998).
[26]A. Goshtasby, "Image registration by local approximation methods," Image Vis. Comput. **6**(4), 255–261 (1988).
[27]See supplementary material at E-MPHYA6-37-047004 for results comparing the alignment accuracy using different MR pulse-sequences and with different transformation methods.
[28]I. P. Witz and O. Levy-Nissenbaum, "The tumor microenvironment in the post-PAGET era," Cancer Lett. **242**(1), 1–10 (2006).
[29]N. Christian *et al.*, "Immobilization device for in vivo and in vitro multimodality image registration of rodent tumors," Radiother. Oncol. **87**(1), 147–151 (2008).
[30]T. Pfluger *et al.*, "Quantitative comparison of automatic and interactive methods for MRI-SPECT image registration of the brain based on 3-dimensional calculation of error," J. Nucl. Med. **41**(11), 1823–1829 (2000).
[31]D. J. Rowland *et al.*, "Registration of [18F]FDG microPET and small-animal MRI," Nucl. Med. Biol. **32**(6), 567–572 (2005).
[32]P. J. Slomka, "Software approach to merging molecular with anatomic information," J. Nucl. Med. **45**, 36S–45S (2004).
[33]B. Jupp and T. J. O'Brien, "Application of coregistration for imaging of animal models of epilepsy," Epilepsia **48**, 82–89 (2007).
[34]D. B. Twieg, "The k-trajectory formulation of the NMR imaging process with applications in analysis and synthesis of imaging methods," Med. Phys. **10**(5), 610–621 (1983).
[35]R. Bowtell and P. Mansfield, "Gradient coil design using active magnetic screening," Magn. Reson. Med. **17**(1), 15–21 (1991).
[36]C. Barmet, N. De Zanche, and K. P. Pruessmann, "Spatiotemporal magnetic field monitoring for MR," Magn. Reson. Med. **60**(1), 187–197 (2008).
[37]C. Barmet *et al.*, "A transmit/receive system for magnetic field monitoring of in vivo MRI," Magn. Reson. Med. **62**(1), 269–276 (2009).
[38]N. G. Papadakis *et al.*, "k-space correction of eddy-current-induced distortions in diffusion-weighted echo-planar imaging," Magn. Reson. Med. **53**(5), 1103–1111 (2005).
[39]P. Blumler *et al.*, *Spatially Resolved Magnetic Resonance: Methods, Materials, Medicine, Biology, Rheology, Geology, Ecology, Hardware* (Wiley-VCH, New York, 1998), Vol. 14, p. 760.
[40]R. W. Brown *et al.*, *Magnetic Resonance Imaging Physical Principles and Sequence Design* (Wiley-Liss, New York, 1999), p. 914.
[41]J.-P. Reveillès, in *The Geometry of the Intersection of Voxel Spaces, Electronic Notes in Theoretical Computer Science*, Vol. **46**, IWCIA, 2001, 8th International Workshop on Combinatorial Image Analysis, (2001), p. 285–308.
[42]J. Montagner, V. Barra, and J.-Y. Boire, "A geometrical approach to multiresolution management in the fusion of digital images," in *Pixelization Paradigm*, Lecture Notes in Computer Science Vol. 4370 (Springer, Berlin/Heidelberg, 2008), pp. 121–136.
[43]J. Guo *et al.*, "In vitro proton magnetic resonance spectroscopic lactate and choline measurements, [18]F-FDG uptake, and prognosis in patients with lung adenocarcinoma," J. Nucl. Med. **45**(8), 1334–1339 (2004).
[44]R. A. Gatenby and R. J. Gillies, "Why do cancers have high aerobic glycolysis?," Nat. Rev. Cancer **4**(11), 891–899 (2004).
[45]A. Buerkle and W. A. Weber, "Imaging of tumor glucose utilization with positron emission tomography," Cancer Metastasis Rev. **27**(4), 545–554 (2008).
[46]K. Brindle, "New approaches for imaging tumour responses to treatment," Nat. Rev. Cancer **8**(2), 94–107 (2008).
[47]G. Agrawal *et al.*, "MRI features of breast cancer: A correlation study with HER-2 receptor," Ann. Oncol. **18**(11), 1903–1904 (2007).
[48]R. Zhou, S. Pickup, T. E. Yankeelov, C. S. Springer, Jr., and J. D. Glickson, "Simultaneous measurement of arterial input function and tumor pharmacokinetics in mice by dynamic contrast enhanced imaging: Effects

of transcytolemmal water exchange," Magn. Reson. Med. **52**(2), 248–257 (2004).
[49]H. Cho *et al.*, "Noninvasive multimodality imaging of the tumor microenvironment: Registered dynamic magnetic resonance imaging and positron emission tomography studies of a preclinical tumor model of tumor hypoxia," Neoplasia, **11**(3), 247–259 (2009).
[50]C. Catana *et al.*, "Rigid-body MR-assisted PET motion correction," J. Nucl. Med. **50**(2), 592 (2009).
[51]M. Hofmann *et al.*, "Towards quantitative PET/MRI: A review of MR-based attenuation correction techniques," Eur. J. Nucl. Med. Mol. Imaging **36**, 93–104 (2009).
[52]R. Weissleder and M. J. Pittet, "Imaging in the era of molecular oncology," Nature (London) **452**(7187), 580–589 (2008).
[53]M. S. Gee *et al.*, "Human breast cancer tumor models: Molecular imaging of drug susceptibility and dosing during HER2/neu-targeted therapy," Radiology **248**(3), 925–935 (2008).
[54]A. M. Wu, "Antibodies and antimatter: The resurgence of immuno-PET," J. Nucl. Med. **50**(1), 2–5 (2009).
[55]D. Artemov *et al.*, "Magnetic resonance molecular imaging of the HER-2/neu receptor," Cancer Res. **63**(11), 2723–2727 (2003).
[56]I. Serganova and R. Blasberg, "Reporter gene imaging: Potential impact on therapy," Nucl. Med. Biol. **32**(7), 763–780 (2005).
[57]B. R. Jarrett *et al.*, "Synthesis of 64Cu-labeled magnetic nanoparticles for multimodal imaging," Bioconjugate Chem. **19**(7), 1496–1504 (2008).